IOP Conference Series:
Earth and
Environmental Science

PAPER • **OPEN ACCESS**

Experimental investigation of a FSFC variable speed pump-turbine prototype – Part2: runner fatigue reduction

To cite this article: D Biner *et al* 2024 *IOP Conf. Ser.: Earth Environ. Sci.* **1411** 012031

IOP Conf. Series: Earth and Environmental Science **1411** (2024) 012031 doi:10.1088/1755-1315/1411/1/012031

Experimental investigation of a FSFC variable speed pump-turbine prototype – Part2: runner fatigue reduction

D Biner[1,3,*], V Hasmatuchi[1], C L Lecointre[1], A Quarroz[1], C Nicolet[2], S Alligné[2], M Dreyer[2], N Hugo[4], D Dujic[3], C Münch-Alligné[1]

[1] Institute of Systems Engineering, School of Engineering, HES-SO Valais-Wallis, Rue de l'Industrie 23, Sion, Switzerland
[2] Power Vision Engineering Sàrl, St-Sulpice, Switzerland
[3] Power Electronics Laboratory – PEL, Ecole Polytechnique Fédérale de Lausanne, Lausanne, Switzerland
[4] Alpiq SA, Lausanne, Switzerland

E-mail: daniel.biner@hevs.ch

Abstract. The demonstration of flexibility technologies to enhance ancillary services of Hydropower Plants (HPPs) is showcased by the XFLEX HYDRO H2020 European Project. The potential of Full Size Frequency Converters (FSFC) is numerically and experimentally assessed by a case study on the Z'Mutt HPP. The investigated unit is a 5 MW variable speed reversible Francis pump-turbine fed by a FSFC that provides full speed control from -100% to +100%, allowing for fast start-up and mitigation of damage caused to different components. In this context, several turbine start-up sequences with controlled guide vane opening and rotational speed are developed, implemented, and tested on prototype scale. The definition of the different sequences, their impact on penstock fatigue and further FSFC capabilities like fast active power control in pump mode and fast power reversion are presented in part 1 of this contribution. Part 2 deals with fatigue damage investigations of the runner with respect to variable speed operation in generating mode using coupled numerical and experimental techniques. Strain signals from the runner blades are extrapolated to the critical areas to assess the relative fatigue damage induced by each turbine start-up. The scaled normal stress approach is applied, which is a critical plane method, adapted for multiaxial stress states. The results reveal that runner damage is mitigated by more than two orders performing a variable speed start-up compared to a classical one with fixed speed technology. Simultaneously, the delay for active power provision is significantly shortened. Thus, the study approves that fast and frequent turbine start-ups are realizable without affecting the runner's service life thanks to the FSFC.

1. Introduction

The improvement of HPPs regarding their provision of Electric Power System (EPS) services remains of high significance in the context of increasing share of New Renewable Energies (NRE) in the energy market. Different technologies to enhance the flexibility of HPPs are demonstrated in the framework of the XFLEX HYDRO H2020 European project [1]. One of the technical configurations investigated is a variable speed pump-turbine unit equipped with a Full Size Frequency Converter (FSFC). This 5 MW pump-turbine unit equipped with a FSFC is part of the Z'Mutt HPP and serves as a test case to investigate the improvements of ancillary

services thanks to variable speed technology. The Z'Mutt HPP is the largest pumping-station of the Grand Dixence hydroelectric complex lain in the Swiss Alps. Frequent provision of active power responses implies increased transient events like start-up and stop cycles as well as operation at partial load. The stress spectrum in grid service mode significantly differs from the one experienced during conventional operation exemplified by [2] and [3]. Accelerated runner cracking due to modified operating schemes is not uncommon as for example investigated by Decaix et al. [4]. The understanding of new load spectra and their impact on service life is therefore essential for safe implementation of advanced ancillary services, for example by quantifying the damage cause by start-up and shut-down cycles as presented by Savin et al. [5]. Furthermore, technologies like FSFC provide a new potential for optimization of operating trajectories for transients like turbine start-ups. A start-up optimization approach is developed for the case study of the Z'Mutt pump-turbine based on preliminary numerical studies [6], [7], [8]. These insights let anticipate that variable speed is beneficial not only for the provision of grid services, but also regarding mitigation of fatigue damage induced on key components like the pump-turbine runners. In the final investigative stage of the Z'Mutt prototype, an experimental campaign is conducted to validate the optimization procedure and numerical results. In part 1 of the paper, 1D hydraulic transient simulations are compared to the on-site test results along with the evaluation of penstock fatigue damage using different control strategies for turbine start-up. The second part of the paper deals with the experimental evaluation of runner fatigue damage complemented by stress extrapolation models from CFD and mechanical FEM simulations. Fatigue damage analyses of hydroelectric runners is a common subject of discussion in the hydropower field. For example, damage assessments of an axial hydraulic turbine runner is presented in [9]. Further, fatigue damage of a Francis runner at off-design conditions is studied by [3], using the concept of relative fatigue damage that allows for a vivid comparison of the added costs. The reliability of coupled CFD-FEM approaches to investigate the mechanical impact of dynamic phenomena in Francis turbines at off-design conditions is demonstrated by [10]. Another example for static and dynamic stress analyses of prototype high head Francis runners based on site measurement is given by [11]. Nevertheless, studies regarding the impact of variable speed and its potential benefit for runner damage only exists in the form of model tests [12] or numerical simulations [13] to the best of the author's knowledge. This paper aims at providing new insights concerning this topic in the particular configuration of a full-size converter fed pump-turbine experimentally studied at prototype scale. A new method to extrapolate the measured strain signals to the hot spot locations is described and a critical plane method to deduce a representative equivalent stress measure for fatigue damage calculations in multiaxial load cases is applied. Finally, runner damage reduction factors comparing different variable speed turbine start-up sequences to the classical fixed speed configuration are provided.

2. Methodology

2.1. Experimental setup

To assess the runner fatigue damage on a wide operating range and during fast transients in turbine mode enabled by FSFC, extensive instrumentation systems are deployed on the stationary and rotating frames of the Z'Mutt pump-turbine prototype. An onboard measurement system is designed and mounted on the tip of the generator shaft to acquire data from the runner instrumentation. Signal transmission wires are passed from the runner nose cone up to the acquisition electronics through the center of the unit's hollow shaft. Illustrations of the onboard measurement system and the instrumented runner are provided in figure 1a. Inter alia, two runner blades are equipped with 18 uniaxial strain gauges and 12 miniature pressure transducers as presented in figure 1b. The blades have been chosen in order to minimize added imbalance since high rotational speeds up to about 1200 1/min are targeted in nominal operating conditions. Additionally, an in-house developed mechanical torque measurement system is

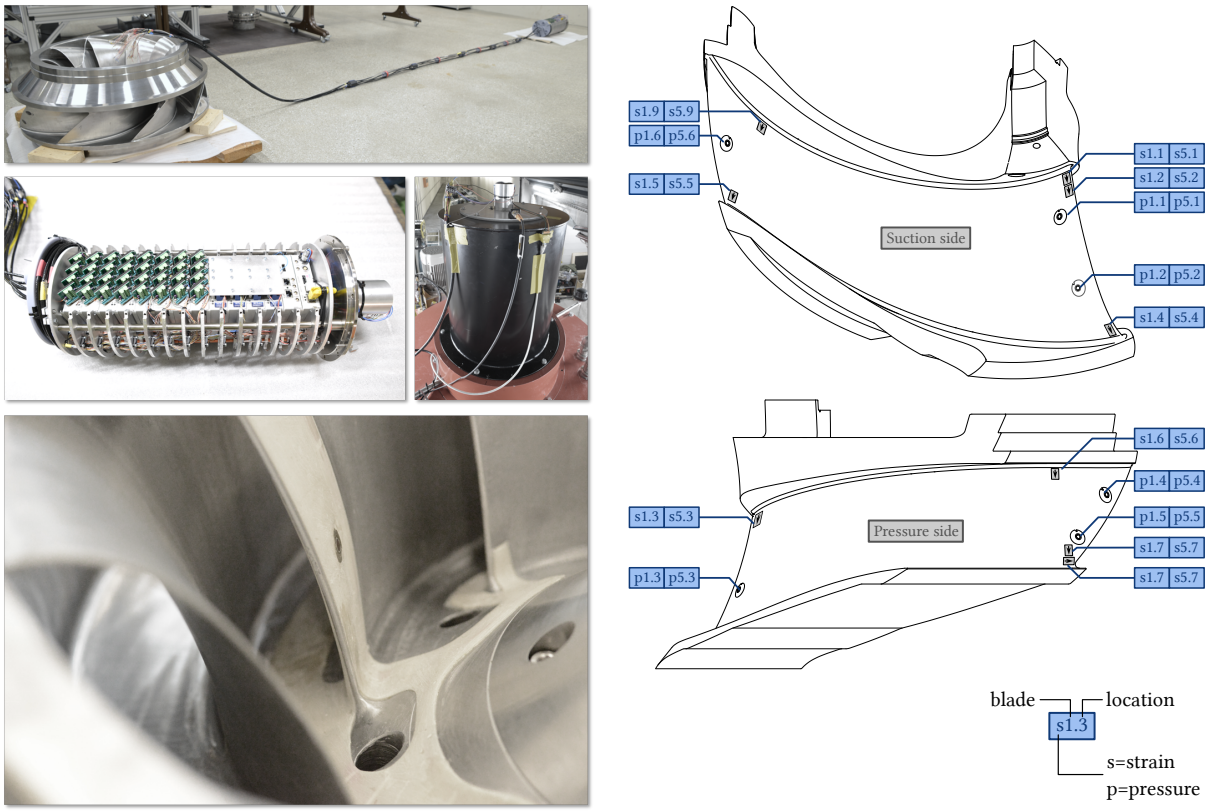

(a) (b)

Figure 1: Illustration of onboard measurement system (a) and indication of sensors installed on the runner blades 1 and 5 (b).

installed to characterize the operating trajectories in the $n_{11} - T_{11}$ frame. An acquisition frequency of 10 kHz is used for relevant dynamic quantities from strain and pressure sensors placed on the runner.

2.2. Numerical setup

To obtain a full picture of experimentally assessed fatigue damage, complementary numerical approaches are typically required since strain gauges can not be installed at the most stressed regions where high curvatures are present. Numerical CFD and FEM models are therefore required to extrapolate measured strains to the critical locations. Since it is necessary to extrapolate the static and dynamic stresses, detailed numerical models are necessary with sufficiently resolved flow structures to extract realistic unsteady pressure fields that are then mapped to transient structural mechanical models. To resolve the flow for a series of stationary turbine operating points, as part of them are shown in figure 3, a mesh with 19.1 M elements is employed, see figure 2a. The SST-SAS turbulence model is used since it is found successful in the prediction of stochastic flow under complex conditions like Speed No-Load (SNL) [14]. The flow is initialized by 14-19 runner revolutions in order to extract converged solutions for 5-7 final rotations, which are used to carry out the one-way coupled Fluid-Structure Interaction simulations. One-way coupling is considered appropriate to determine stress extrapolation functions, since they depend on the strain distribution and not on the absolute strain values that are subjected to the exact damping in case of resonance conditions. The temporal resolution

for the final revolutions corresponds to 0.9 degrees of runner rotation. More details on the CFD setup employed for this study can be found in [15]. A transient structural runner model is created composed of 1.03 M elements including the acoustic domains inside the runner blade channels and the labyrinth gaps. Moreover, the shaft line geometry is partially modeled in order to capture bending and torsional dynamics, see figure 2b. The FEM mesh is periodic implying identical refinements at all strain gauge locations and stress concentration areas. The periodic grid enables to extract identically accurate solutions from each runner blade that is advantageous to increase the statistical significance of the numerical results. Details of the grid at the most relevant fatigue hot spot locations are shown in figure 2c including the indications of the strain gauge positions. The illustrated regions hs-1 and hs-3 correspond to the leading edge shroud transition and the trailing edge hub transition, respectively.

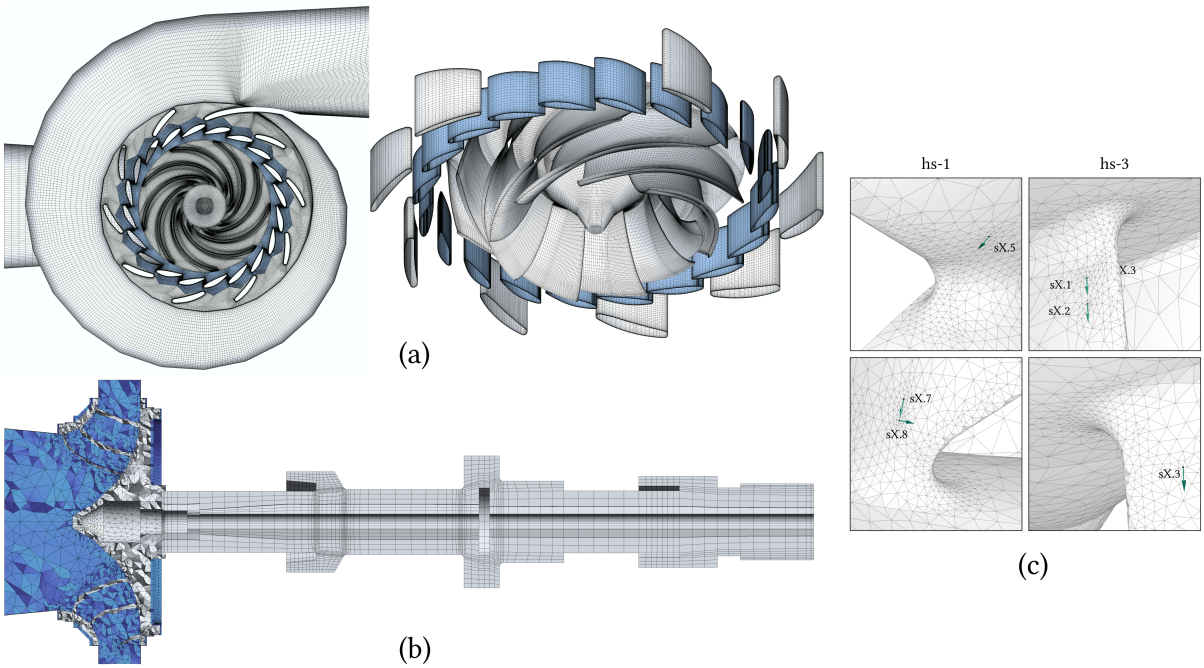

Figure 2: Computational grids for unsteady CFD (a) and transient structural FEM (b) simulations with details on refinements on the critical spots and strain gauge locations (c).

2.3. Stress extrapolation

This section covers the methodology used to correlate the measured strain signals with the stresses at the fatigue hot spot regions by means of transient FEA results. For this purpose, the stress fields are separated into static parts from centrifugal forces and the time averaged pressure field, and dynamic parts from pressure fluctuations and/or structural resonance, see (1). It is assumed that the stress fields induced by each effect exhibit a different shape, which consequently means that extrapolation factors are different for each component. The problem can be simplified since it is reasonable to cluster the two static stress components. For a given machine at identical hydraulic conditions ($[n_{11}, Q_{11}]$ = cst.), centrifugal and static pressure stresses behave approximately proportional to the net head considering Francis type turbines dedicated to medium to high heads. This property is demonstrated in (2) to (4) adopting the stress scaling factor described by Valentin et al. [16], here denoted as $\lambda_{\sigma_{\overline{p}}}$. This means that the proportions between the centrifugal and the static pressure stresses remain constant regardless

variations of the head. Consequently, constant stress extrapolation factors for the total static stress components can be specified for a given hydraulic characteristics set point.

$$\underline{\underline{\sigma}} = \underbrace{\underline{\underline{\sigma}}_{\Omega}}_{\text{rotation}} + \underbrace{\underline{\underline{\sigma}}_{\overline{p}}}_{\text{stat. pressure}} + \underbrace{\underline{\underline{\sigma}}_{dyn}}_{\text{dynamic}} = \underline{\underline{\sigma}}_{stat} + \underline{\underline{\sigma}}_{dyn} \tag{1}$$

$$\lambda_{n_{11}} = 1 = \frac{\frac{\Omega_2 D_2}{\sqrt{H_2}}}{\frac{\Omega_1 D_1}{\sqrt{H_1}}} = \frac{\lambda_\Omega}{\sqrt{\lambda_H}} \rightarrow \lambda_\Omega = \sqrt{\lambda_H} \quad \text{if} \quad D_1 = D_2 \tag{2}$$

$$\lambda_{\sigma_{\overline{p}}} = \lambda_{C_p}\, \lambda_E = \frac{\frac{\Delta p_2}{\rho_2 E_2}}{\frac{\Delta p_1}{\rho_1 E_1}} \frac{E_2}{E_1} = \frac{\Delta p_2}{\Delta p_1} = \lambda_{\Delta p} \approx \lambda_H \quad \text{if} \quad \rho_1 = \rho_2 \tag{3}$$

$$\lambda_{\sigma_\Omega} = \lambda_\Omega^2 = \lambda_H \rightarrow \lambda_{\sigma_\Omega} \approx \lambda_{\sigma_{\overline{p}}} \tag{4}$$

Since stress distributions induced by static and dynamic loads may be different, stress extrapolation must be performed individually for each part. Furthermore, the structural simulations reveal important stress multiaxiality in the critical regions, especially at location hs-1 at the leading edge shroud transition. Thus, a methodology to extrapolate the full stress tensor is proposed. This implies that extrapolation is performed for all tensorial components using either a simple linear correlation for the static part (5) or a linear combination of multiple measured strain signals for the dynamic part (6), where Y is the Young's modulus applied to obtain dimensionless extrapolation factors, and $\varepsilon_{\text{sg,stat}}$ and $\varepsilon_{\text{sg,dyn}}$ are the static and dynamic strain gauge signals respectively. Further, i and j denote the strain gauge indices used to extrapolate the static and dynamic parts respectively.

$$\underline{\underline{\sigma}}_{\text{e,stat}} = Y\, \varepsilon_{\text{sg,stat}}^{(i)}\, \underline{\underline{K}}_{\text{stat}}^{(i)} \qquad \underline{\underline{K}}_{\text{stat}} = \begin{bmatrix} K_{\text{stat},(1,1)} & K_{\text{stat},(1,2)} & K_{\text{stat},(1,3)} \\ K_{\text{stat},(2,1)} & K_{\text{stat},(2,2)} & K_{\text{stat},(2,3)} \\ K_{\text{stat},(3,1)} & K_{\text{stat},(3,2)} & K_{\text{stat},(3,3)} \end{bmatrix} \tag{5}$$

$$\underline{\underline{\sigma}}_{\text{e,dyn}}(t) = Y \sum_{j=1}^{J} \varepsilon_{\text{sg,dyn}}^{(j)}(t)\, \underline{\underline{K}}_{\text{dyn}}^{(j)} \qquad \underline{\underline{K}}_{\text{dyn}} = \begin{bmatrix} K_{\text{dyn},(1,1)} & K_{\text{dyn},(1,2)} & K_{\text{dyn},(1,3)} \\ K_{\text{dyn},(2,1)} & K_{\text{dyn},(2,2)} & K_{\text{dyn},(2,3)} \\ K_{\text{dyn},(3,1)} & K_{\text{dyn},(3,2)} & K_{\text{dyn},(3,3)} \end{bmatrix} \tag{6}$$

Note that the extrapolation matrices are symmetric as the stress tensor is. Thus, the method requires to fit totally $6 + J \cdot 6$ unknowns to establish the extrapolation model, where J is the number of strain gauges used for the dynamic part. The stress tensor in the vicinity of the measurement points based on experimental strain signals is finally reconstructed as follows:

$$\underline{\underline{\sigma}}_{\text{e,exp}} = Y \left(\varepsilon_{\text{sg,stat,exp}}^{(i)}\, \underline{\underline{K}}_{\text{stat}}^{(i)} + \sum_{j=1}^{J} \varepsilon_{\text{sg,dyn,exp}}^{(j)}\, \underline{\underline{K}}_{\text{dyn}}^{(j)} \right) \tag{7}$$

The dynamic stress extrapolation matrices are fit by optimization techniques using transient FEA solutions. The objective function is based on the coefficient of determination (R^2) between the extrapolated and the accurate solution, combined with a penalty function to conserve the maximum dynamic stress amplitude appearing in the simulated time series. The static extrapolation matrix can explicitly be calculated using time averaged FEA results. A limiter for the static extrapolation factors should be considered since equilibrium states may be present where strains tend to zero. The stress extrapolation factors may vary as function of the operating point, which implies that interpolation models for static and dynamic extrapolation factors need to be defined as function of n_{11} and T_{11} or Q_{11} in order to deduce stresses during transient

operation. The stress tensor extrapolated to the suspected fatigue hot spot region can then be transformed to any appropriate equivalent uniaxial stress measure used as an input for the fatigue damage model. Since stress measures like Von Mises, signed Von Mises or even the first principal stress are not generally representative for fatigue damage calculations in multiaxial or even non-proportional load cases, the scaled normal stress approach proposed by Gaier et al. [17], [18] and reviewed by Wächter et al. [19] is adopted. This method yields a scaling factor applied to the stress tensor as function of a multiaxiality criterion. Subsequently, the orientation of the maximum damage plane is determined by a search algorithm. Hence, the normal stress in the direction where maximum fatigue damage occurs is considered for the fatigue damage evaluation. This scaled stress component normal to the maximum damage plane is here denoted as σ_n. The fatigue evaluation is based on a stress-life curve reproduced from [20] assuming Palmgren-Miner's hypothesis to sum the damages from individual stress cycles identified by rainflow counting.

3. Results

3.1. Start-up trajectories and stationary operating points

The FSFC capability is used to perform precise operating trajectories during turbine start-up by controlling the rotational speed and the guide vane opening simultaneously. The different sequences are named according to their respective objective. Please consider part 1 of the paper for detailed information on the trajectory definitions. Seven start-up trajectories are experimentally assessed on the prototype which are outlined in figure 3, characterized by the torque factor T_{11} deduced from a mechanical torque sensor as well as the discharge factor Q_{11} based on the Winter-Kennedy method. The stationary operating points experimentally and numerically investigated are indicated in the $n_{11} - Q_{11}$ plot. Due to unexpected delays in the control loop of the rotational speed, slight deviations between expected and measured trajectories occurred. These issues could not be solved within the limited time slot of the experimental campaign. Nevertheless, as reported in part 1 of the paper, the agreement between transients predicted by 1-D hydraulic simulations and the experiments is considered acceptable. Note that the fixed speed start-up trajectory is measured in two steps since the activation of the frequency converter was not possible during rotation of the shaft line.

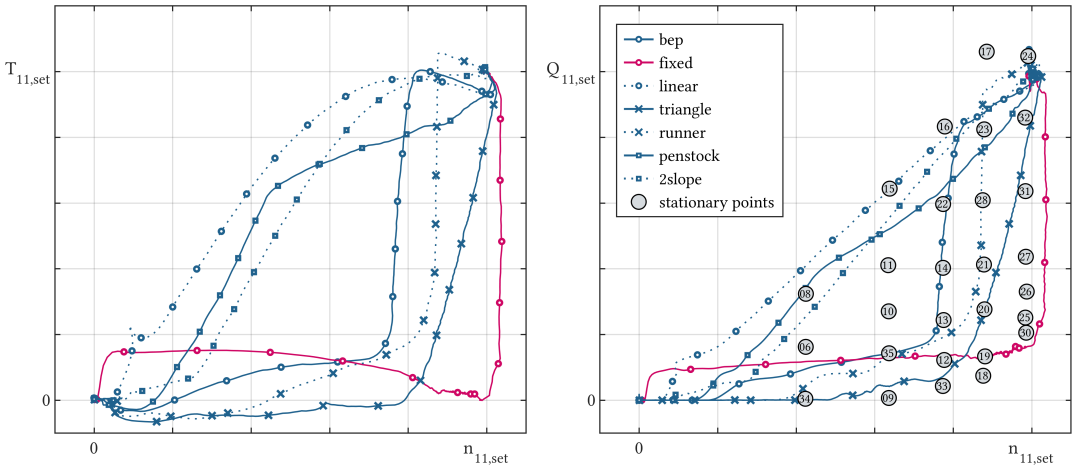

Figure 3: Measured start-up trajectories in form of $n_{11} - T_{11}$ (left) and $n_{11} - Q_{11}$ (right) characteristics with indication of stationary operating points.

3.2. Comparison between measured and simulated strains

The static and dynamic strain correlations between simulated and measured values for the most relevant sensors s1.1, s1.2 and s1.5 are outlined in figure 4. Only the results from blade number 1 are indicated, but it should be noted that no significant differences are observed between redundant sensors at fixed operating conditions. This fact confirms the proper installation and response of the strain gauges. The dynamic strains correspond to the peak-to-peak values determined using a probability distribution function with a value of 99%. According to IEC TS 62882:2020 [21], a probability value of 97% is proposed to determine peak-to-peak values of pressure fluctuations. A slightly larger probability is chosen for this work to reduce filtering effect of experimental outliers in order to increase the evidence of the simulated strain fluctuations. The numerical peak-to-peak values are obtained using the strain gauge results from all 9 runner blades to maximize the simulated statistical content. The static strains tend to be underestimated by simulation, but tendencies are acceptably well reproduced for the different operating conditions. Static strains s1.2 and s1.5 exhibit a better correlation compared to s1.1. Regarding the dynamic strains, some significant differences can be observed for the sensors located at the blade trailing edge. Small fluctuations are underestimated by simulation, whereas the numerical models overestimate the large ones. The agreement between the dynamic strains at the blade leading edge is excellent, whereby the same tendency to obtain rather conservative predictions for high peak-to-peak values are observed.

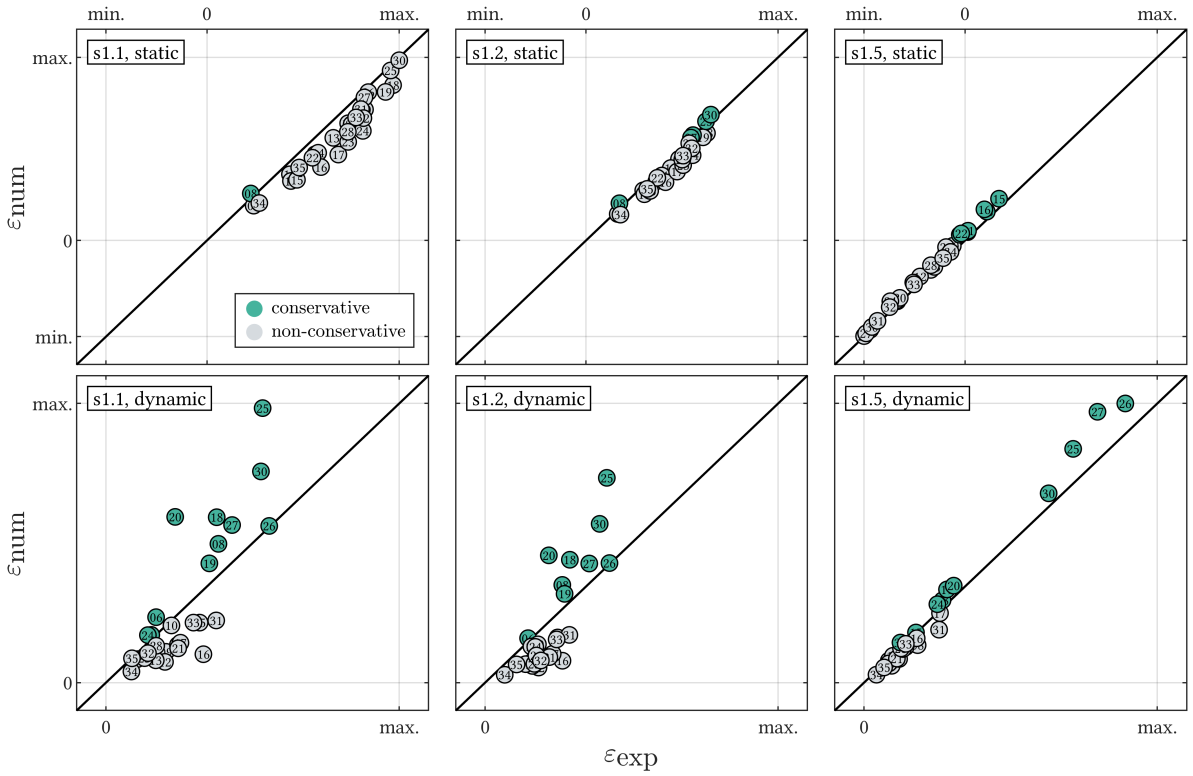

Figure 4: Comparison between measured and simulated dynamic and static strains for all tested stationary operating points based on results from blade number 1.

3.3. Runner fatigue damage

The equivalent stress component σ_n normal to the maximum damage planes, whose orientations are identified by simulation, is deduced from the extrapolated stress tensors based on the

measured strain signals. This operation is performed for all locations of the FEM grid nodes in the vicinity of the strain gauges. Consequently, the accumulated damage during each of the start-up sequences can be assessed on the surfaces in the critical zones rather than at a single location. Note that extrapolation matrices need to be individually calibrated for each considered grid node. Examples of the evolution of the equivalent stress at the maximum damage points in regions hs-1 and hs-3, which turned out to be the most relevant ones, as well as the resulting relative accumulated fatigue damages are illustrated in figure 5. The illustration shows the most damaging case represented by the fixed speed sequence and the most beneficial case in terms of damage reduction given by the "runner" sequence. The damage values are standardized by the maximum value induced during the fixed speed start-up in the region hs-1. Axes limits correspond to the minimum and maximum stresses detected among all tested strategies. As clearly visible, large stresses maxima inducing low fatigue cycles and significant stress fluctuations inducing high fatigue cycles occur during the fixed speed start-up. These two effects are both mitigated by performing a start-up with variable speed. Furthermore, stresses extrapolated to the same spots from different sensors are in quite good agreement, indicating to some extent the correct response of the strain gauges as well as the validity of the extrapolation method.

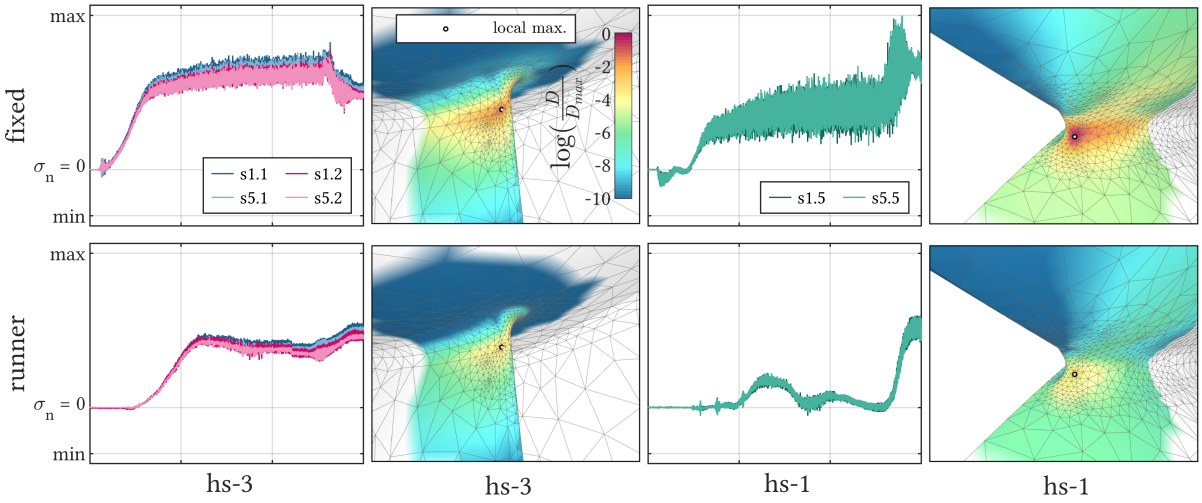

Figure 5: Extrapolated stresses at maximum damage points deduced from measured strain signals and corresponding accumulated fatigue damages of the most (fixed) and least (runner) damaging start-up sequence.

Finally, the damage reduction factors linked to each of the variable speed trajectories are calculated. These values indicate the number of start-ups needed to create a runner damage equivalent to one fixed speed start-up. The location specific damage reduction factors deduced from different strain sensors are presented in table 1 and figure 6. Some non-neglectable differences are observed between redundant sensors, for example during the "runner" sequence at hs-1. Deeper analyses are required to identify the source of these discrepancies, but it is suspected that they are rather of physical nature than related to measurement uncertainties since deviations are not systematic. Mode shapes creating non-identical stress fields on each blade or hydrodynamic instabilities leading to flow asymmetries in the blade channels may be part of the explanation. Considering the potential of damage reduction with FSFC, significant improvements are achieved, especially at the leading edge shroud transition with a maximum damage reduction factor of 361. This trajectory is established with the objective to minimize the runner damage based on preliminary CFD/FEM calculations, as explained in part 1 of the

paper. Indeed, this sequence turned out the most beneficial one according to the experimental outcomes.

Table 1: Identified damage reduction factors for each start-up trajectory at hot spot locations hs-1 and hs-3.

	hs-3				hs-1	
	s1.1	**s5.1**	**s1.2**	**s5.2**	**s1.5**	**s5.5**
fixed	1	1	1	1	1	1
linear	20	16.8	21.1	22.2	33.1	32.6
runner	34.5	25.5	29.6	37.9	256.7	361.1
2slope	35.7	29.6	32.4	34.4	178.6	134.7
penstock	35.8	33.9	27.6	34.2	111	118.9
triangle	32.7	33.6	26.9	30.6	66.3	59
bep	40.2	33.1	34.9	39.5	77.8	110.2

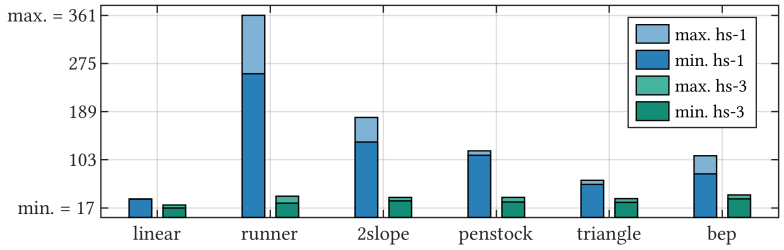

Figure 6: Range of experimentally determined damage reduction factors for the two relevant hot spot regions.

4. Conclusions

The evidence of fast and safe turbine start-up capabilities of a full-size converter fed Francis pump-turbine prototype is demonstrated by means of coupled numerical and experimental methods. Detailed investigations of the runner fatigue damage induced by different start-up control sequences following a defined operating trajectory are carried out based on a stress-life model. A stress extrapolation methodology is proposed that permits the reconstruction of the full stress tensor in the vicinity of the strain gauge locations. Since important multiaxial stress states are identified at one of the hot spot regions at the transition between the blade leading edge and the runner shroud, the scaled normal stress approach is applied to obtain an equivalent uniaxial stress measure more appropriate for fatigue damage calculations compared to conventional definitions. Measured strains are extrapolated to the FEM grid nodes in the critical regions to reveal accumulated damages on the blade geometry. The damage reduction factors from different speed control strategies in relation to the conventional fixed speed scenario are presented. The operating trajectory dedicated to minimize the runner fatigue established by preliminary numerical investigations indeed exhibits the largest damage reduction factor of 361 at the leading edge shroud transition. It is demonstrated that the risk of runner cracking due to start-up in generating mode is significantly reduced using FSFC solutions. This enables

the possibility to increase the number of start-up events for the provision of large active power responses without curtailments of the runner service life.

Acknowledgments
The Hydropower Extending Power System Flexibility (XFLEX HYDRO) project has received funding from the European Union's Horizon 2020 research and innovation programme under grant agreement No 857832. The authors would like to thank CKD Blansko, Grand Dixence SA and Hydro Exploitation SA for their collaboration and support. This work is carried out using Ansys software from Ansys Inc.

References

[1] XFLEX HYDRO Hydropower Extending Power System Flexibility (XFLEX HYDRO) https://xflexhydro.net/ (accessed Jun. 09, 2024)
[2] J Löfflad and M Eissner 2014 Life time assessment and plant operation optimization based on geometry scan and strain gauge testing – start/stop optimization *IGHEM 2014*
[3] Monette C, Marmont H, Chamberland-Lauzon J, Skagerstrand A, Coutu A and Carlevi J 2016 *IOP Conference Series: Earth and Environmental Science* **49** 072018 URL https://dx.doi.org/10.1088/1755-1315/49/7/072018
[4] Decaix J, Hasmatuchi V, Titzschkau M, Rapillard L, Manso P, Avellan F and Münch-Alligné C 2019 *IOP Conference Series: Earth and Environmental Science* **240** 082014 URL https://dx.doi.org/10.1088/1755-1315/240/8/082014
[5] Savin O, Baroth J, Badina C, Charbonnier S and Bérenguer C 2021 *International Journal of Fatigue* **153** 106458 ISSN 0142-1123 URL https://www.sciencedirect.com/science/article/pii/S0142112321003169
[6] Alligné S, Béguin A, Biner D, Münch-Alligné C, Hasmatuchi V, Hugo N, Avellan F, Dujic D and Nicolet C 2021 *IOP Conf. Series: Earth and Environmental Science 774 (2021) 012052*
[7] Biner D, Alligné S, Hasmatuchi V, Nicolet C, Hugo N, Avellan F, Dujic D and Münch-Alligné C 2021 *IOP Conf. Series: Earth and Environmental Science 774 (2021) 012070*
[8] Biner D, Alligné S, Hasmatuchi V, Nicolet C, Dujic D and Münch-Alligné C 2022 *IOP Conf. Series: Earth and Environmental Science 774 (2021) 012070*
[9] Monette C, Chamberland-Lauzon J and Nennemann B 2022 *IOP Conference Series: Earth and Environmental Science* **1079** 012100 URL https://dx.doi.org/10.1088/1755-1315/1079/1/012100
[10] Duparchy F, Brammer J, Thibaud M, Favrel A, Lowys P Y and Avellan F 2017 *Journal of Physics: Conference Series* **813** 012035
[11] Huang X, Oram C and Sick M 2014 *IOP Conference Series: Earth and Environmental Science* **22** 032052 URL https://dx.doi.org/10.1088/1755-1315/22/3/032052
[12] Seydoux M, Vagnoni E, Nicolet C, Alligné S, Hugo N and Paolone M 2022 *IOP Conference Series: Earth and Environmental Science* **1079** 012105
[13] Pacot O, Delannoy J, André F, Segoufin C, Delgado J, Roque M and Münch-Alligné C 2022 *IOP Conf. Ser.: Earth Environ. Sci. 1079 012069*
[14] Nennemann B, Morissette J, Chamberland-Lauzon J, Monette C, Braun O, Melot M, Coutu A, Nicolle J and Giroux A 2014 *IOP Conf. Series: Earth and Environmental Science 22 (2014) 032055*
[15] Biner D, Dujic D and Münch-Alligné C 2023 Numerical study on pressure fluctuations in a variable speed pump-turbine with head variations *Proceedings of the 9th IAHR Meeting of the Work Group on Cavitation and Dynamic Problems in Hydraulic Machinery and Systems*
[16] Valentin D, Presas A, Valero C, Egusquiza M, Egusquiza E, Gomes J and Avellan F 2020 *Renewable Energy* **152** 1011–1023
[17] Gaier C and Dannbauer H 2005 An efficient critical plane method for ductile, semi-ductile and brittle materials URL https://api.semanticscholar.org/CorpusID:14256777
[18] Gaier C and Dannbauer H 2008 *The Arabian Journal for Science and Engineering* **33**
[19] Wächter M, Linn A, Wuthenow R, Esderts A, Gaier C, Kraft J, Fällgren C and Vormwald M 2022 *Applied Mechanics* **3** 259–295 ISSN 2673-3161 URL https://www.mdpi.com/2673-3161/3/1/18
[20] Sonsino C M and Dieterich K 1990 *Werkstoffe und Korrosion* **41** 330–342
[21] IEC TS 62882:2020 , Hydraulic machines - Francis turbine pressure fluctuation transposition